Entangled quantum cellular automata, physical complexity, and Goldilocks rules

Logan E. Hillberry,[1,2] Matthew T. Jones,[1] David L. Vargas,[1] Patrick Rall,[3,4] Nicole Yunger Halpern,[4,5,6,7] Ning Bao,[4,8] Simone Notarnicola,[9,10] Simone Montangero,[10,11,12] and Lincoln D. Carr[1]

[1]*Department of Physics, Colorado School of Mines, Golden, CO 80401, USA*
[2]*Center for Nonlinear Dynamics, The University of Texas at Austin, Austin, TX 78712, USA*
[3]*Quantum Information Center, The University of Texas at Austin, Austin, TX 78712, USA*
[4]*Institute for Quantum Information and Matter,*
California Institute of Technology, Pasadena, CA 91125, USA
[5]*Harvard-Smithsonian Center for Astrophysics, Cambridge, MA 02138, USA*
[6]*Department of Physics, Harvard University, Cambridge, MA 02138, USA*
[7]*Research Laboratory of Electronics, Massachusetts Institute of Technology, Cambridge, MA 02139, USA*
[8]*Berkeley Center for Theoretical Physics, University of California, Berkeley, CA 94720, USA*
[9]*Dipartimento di Fisica e Astronomia, Università degli Studi di Padova, I-35131 Italy*
[10]*Istituto Nazionale di Fisica Nucleare (INFN), Sezione di Padova, I-35131 Italy*
[11]*Dipartimento di Fisica e Astronomia, Università degli Studi di Padova, I-35131 Italy*
[12]*Theoretische Physik, Universität des Saarlandes, D-66123 Saarbrücken, Germany*
(Dated: May 18, 2020)

Cellular automata are interacting classical bits that display diverse behaviors, from fractals to random-number generators to Turing-complete computation. We introduce entangled quantum cellular automata subject to Goldilocks rules, tradeoffs of the kind underpinning biological, social, and economic complexity. Tweaking digital and analog quantum-computing protocols generates persistent entropy fluctuations; robust dynamical features, including an entangled breather; and network structure and dynamics consistent with complexity. Present-day quantum platforms—Rydberg arrays, trapped ions, and superconducting qubits—can implement Goldilocks protocols, which generate quantum many-body states with rich entanglement and structure. Moreover, the complexity studies reported here underscore an emerging idea in many-body quantum physics: some systems fall outside the integrable/chaotic dichotomy.

I. INTRODUCTION: PHYSICAL COMPLEXITY IN QUANTUM SYSTEMS

Classical cellular automata evolve bit strings (sequences of 1s and 0s) via simple rules that generate diverse emergent behaviors. *Quantum* cellular automata (QCA) evolve quantum bits (qubits), supporting superpositions and entanglement (See 1). In computer science, complexity characterizes the number of steps in an algorithm. The algorithmic-complexity perspective on cellular automata has received much attention [1]. In contrast, physical complexity characterizes emergent behaviors, such as materials' rigidity, spontaneous symmetry breaking [2], and self-organized criticality. Biological, social, and economic complexity features complex networks, natural selection, diversity, power-law statistics, and robustness-fragility tradeoffs [3, 4]. Does the complexity arise in the quantum regime, or only at classical and biological scales?

We study QCA's physical complexity [9–11], identifying *Goldilocks* QCA rules that enforce tradeoffs. These rules generically generate complexity, quantified with the quantum generalizations of measures used in electroencephalogram/functional-magnetic-resonance-imaging (EEG/fMRI) measurements of the brain [12]: mutual-information complex networks. Non-Goldilocks QCA tend toward equilibration, whereas Goldilocks QCA generate (i) robust dynamical features, (ii) persistent entropy fluctuations, (iii) average complex-network measures consistent with classical complexity, and (iv) nontrivial network and entanglement dynamics. Such systems, we show, can be created on present-day analog quantum-computers, or quantum simulators [6]: Rydberg atoms in optical lattices [7, 13] and trapped ions [14, 15]. Our QCA can also be implemented on digital-quantum-computing platforms, including superconducting qubits, used to demonstrate quantum supremacy [16]. Quantum simulators [6, 17, 18] have energized the developing field of nonequilibrium quantum dynamics [19]. Our work provides a direction for such exploration, a physical question: the origins of features discovered in multiscale complexity science, which, we show, occur in simple, abiological quantum systems.

We emphasize physical complexity in our work because many early QCA studies spotlighted single-particle or semiclassical approximations [1, 20–22] or weak correlations at the level of density functional theory [23, 24]. Another line of work has highlighted Clifford operators [25–28], which can efficiently be simulated classically [29]. Our QCA generate states whose quantum entropies scale in a manner between area and volume laws and remain exceptionally structured and dynamic. Therefore, semiclassical QCA have little relevance to our study of physical complexity. Other entangled QCA appear in the literature, such as in [9], which concerns the entanglement generated from specific initial conditions by a single QCA model within our paradigm, in [30], which concerns information transport and entanglement distribution, and
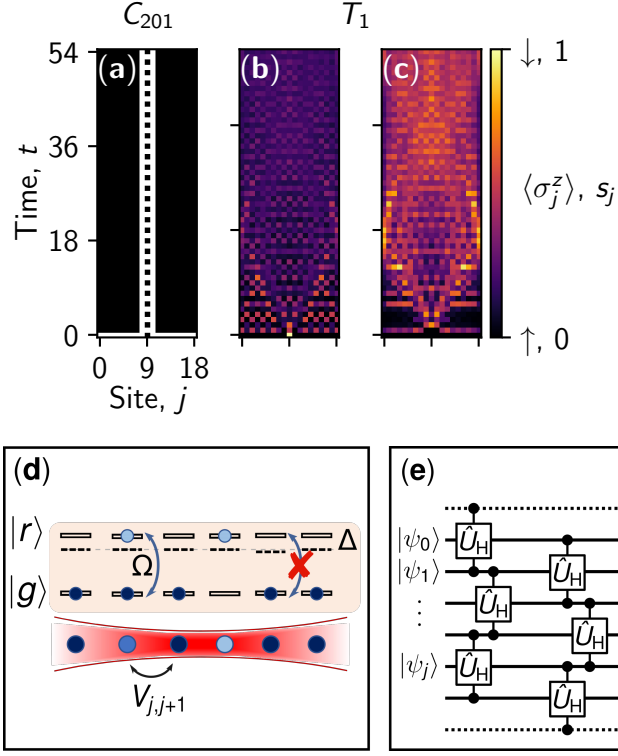
FIG. 1. (a) The classical-elementary-cellular-automaton [5] rule C_{201} flips a classical bit (black=1, white=0) if and only if its nearest neighbors are 0s. This L=19-site chain is initialized with a 1 centered in 0s. A periodic pattern, called a blinker, propagates upward in discrete time steps. (b) We extend C_{201}, for QCA, to rule T_1. The classical bit becomes a quantum bit in an L=19-site chain. The average spin $\langle \hat{\sigma}_j^z \rangle$ has richer discrete-time dynamics, oscillating between the classical extremes of 0 (black) and 1 (white) and filling the lattice. A truly quantum analog of the classical blinker—a quantum entangled breather—appears in Figs. 2(g)-(h). (c) The quantum lattice evolves into a high-entropy entangled state. s_j denotes the site-j second-order Rényi entropy, routinely measured in quantum simulators [6]. (d) Such an analog quantum computer has implemented rule T_1, recently named the PXP model. Optical tweezers were used to trap a Rydberg-atom chain [7, 8]. (e) A quantum circuit can realize digital T_1 dynamics. One QCA time step requires two layers of controlled-controlled-Hadamard gates. The first layer evolves even-index qubits; and the second, odd-index. The dashed line represents the boundary qubits, which remain fixed in $|0\rangle$'s.

in [31–34], which studies entanglement growth in Clifford and Clifford-like QCA. Some experimental work has touched upon QCA-like systems including nuclear magnetic resonance studies on three-spin molecules [35] and the PXP model realized in Rydberg atom chains [7]. However, QCA's physical complexity has not been addressed.

This paper is organized as follows. Section II overviews the time-evolution protocols in our QCA models. With this high-level understanding in place, Section III demonstrates our central claim: Goldilocks QCA generate physical complexity despite their simple underlying structure, based in unitary quantum mechanics. Sections II-III suffice for grasping the power of Goldilocks to QCA to produce complexity. For those who wish to reproduce our work completely and understand every aspect, our QCA models' mathematical details are described in Section IV; and our quantifiers, in Section V. In Section VI, we propose a physical implementation of our models in Rydberg systems, an experimentally realized quantum simulator [6]. In section VII, we conclude with this work's significance.

II. OVERVIEW OF DISCRETE AND CONTINUOUS QCA

The best-known classical cellular automata are the *elementary cellular automata* (ECA), one-dimensional length-L bit strings. Each bit updates in discrete time steps, according to a function defined on the bit's neighborhood. The neighborhood is defined as the bit and its nearest neighbors. The 256 possible transition functions are encoded in the *rule number*, $C_R = 0, 1, \ldots, 255$. A time step t ends when all bits have been updated. Rule C_{110} is Turing-complete, or capable of simulating any computer program.

Our entangled QCA are one-dimensional. They extend ECA's neighborhood-dependent update rule while remaining spatially discrete. Five new features distinguish QCA: First, the classical bit is traded for a qubit parameterized by two angles: $\cos(\theta/2) |0\rangle + e^{i\phi} \sin(\theta/2) |1\rangle$, wherein $|0\rangle$ and $|1\rangle$ denote the ± 1 eigenstates of the Pauli z-operator, $\hat{\sigma}^z$, and $\theta, \phi \in \mathbb{R}$. Second, time updates entangle qubits. The entanglement generates quantum entropy and long-range nonlocal features absent from ECA. Third, our QCA can run in discrete or continuous time. Hence QCA can be implemented on digital and analog quantum computers. Fourth, updates can depend on more neighbors, ≤ 4. Fifth, in digital QCA, all sites cannot update simultaneously, due to the no-cloning theorem. Site updates within a time step must be ordered. Similarly, the update of a site must not depend on the site itself. Our digital three-site QCA therefore parallel the 16 locally invertible ECA.

Section IV will detail our QCA mathematically. Briefly, each QCA is defined by a rule number that encodes under what conditions on a qubit's neighbors the qubit evolves nontrivially. Site j has a set Ω_j of neighbors: the sites, excluding j, within some radius r of j. The boundary conditions are fixed: For sites within $< r$ sites of a boundary, we imagine neighbors extending to additional sites fixed to $|0\rangle$'s. Ω_j corresponds to a Hilbert space on which is defined a vector space spanned by projectors $\hat{\mathcal{P}}_{\Omega_j}^{(i)}$. The i enumerates the neighbors' possible configurations, and $\sum_i \hat{\mathcal{P}}_{\Omega_j}^{(i)} = \hat{\mathbb{1}}$.

To define digital time evolution, we convert an ECA

rule number into a neighborhood-sized unitary gate. The gate evolves different neighborhoods in different circuit layers, in a time-ordering scheme illustrated in Fig. 1(e). The single-neighborhood unitary has the form

$$\hat{U}_j = \sum_i \hat{V}_j^{c_i} \hat{\mathcal{P}}_{\Omega_j}^{(i)}. \tag{1}$$

$\hat{V}_j$ denotes a unitary activation operator on site j. The rule number's binary expansion determines the $c_i \in \{0, 1\}$. The matrix power implies that $\hat{V}^{c_i} \in \{\hat{\mathbb{1}}, \hat{V}\}$. We illustrate with radius-1 digital QCA whose activation is the Hadamard gate (the Bloch-sphere rotation that interchanges the x- and z-axes) times a phase gate (which rotates about the z-axis). Even-j sites are updated first; and odd-j sites, second [Fig. 1(e)]. We denote these QCA by T_R. T evokes three-site neighborhoods, and $R = 0, 1, \ldots, 15$ denotes the rule number.

To define analog time evolution, we convert the rule number into a many-body Hamiltonian $\sum_j \hat{H}_j$. The single-neighborhood Hamiltonian

$$\hat{H}_j = \hat{h}_j \sum_i c_i \hat{\mathcal{P}}_{\Omega_j}^{(i)}. \tag{2}$$

$\hat{h}_j$ denotes a Hermitian activation operator. The rule number's binary expansion determines the $c_i \in \{0, 1\}$. We explore analog, radius-2, totalistic QCA with activation $\hat{h}_j = \hat{\sigma}_j^x$, the Pauli x-operator. Totalistic rules update a neighborhood's central site conditionally on the total number of neighbors in $|1\rangle$. We denote these simulations by F_R. F refers to five-site neighborhoods; $R = 0, 1, \ldots, 31$ denotes the totalistic rule number.

An example QCA is the Goldilocks rule T_6. The local update unitary has the form $\hat{U} = \hat{P}^{(0)} \otimes \hat{U}_H \otimes \hat{P}^{(1)} + \hat{P}^{(1)} \otimes \hat{U}_H \otimes \hat{P}^{(0)}$. The $\hat{P}^{(m)} = |m\rangle\langle m|$ for $m = 0, 1$ are the projectors onto the single qubit $\hat{\sigma}_z$ eigenspace. The activation operator, the Hadamard gate $U_H = (\hat{\sigma}^z + \hat{\sigma}^x)/\sqrt{2}$, acts if exactly one neighbor is in $|1\rangle$—not zero (too few) or two (too many); hence the name "Goldilocks." Such tradeoffs generate and maintain complexity [36]. We explored diverse digital and analog activation operators, site-update orderings, boundary conditions, and neighborhoods. Complexity outcomes, quantified with entropy fluctuations and network structure and dynamics, were always similar. This Report summarizes our findings with a few representative cases. Only Goldilocks rules produce complexity, defined below, independently of all other variables.

Figure 1(a) features the ECA rule C_{201}, well-known to produce a periodic pattern called a *blinker*. The equivalent digital QCA rule, T_1, generates Figs. 1(b)-(c). T_1 produces richer dynamics, including the generation of quantum entropy. The analog version of T_1 is the PXP model [7], realized with Rydberg-excited neutral atoms [Fig. 1(d)]. Such models display diverse quantum dynamical features, including many-body scars [37]. The important point is that a QCA has been created experimentally. However, it is not widely realized that the PXP model is a QCA, albeit not a Goldilocks rule. In this analog QCA, the activation operator, a spin flip, acts if and only if no neighbor occupies $|1\rangle$. Adding a longitudinal field to a common quantum-simulator Hamiltonian, the transverse-field Ising model suffices to realize more-general QCA. We propose an implementation of the five-site F-rules in Rydberg-atom chains in Fig. 9 of Section VI.

III. DEMONSTRATION: GOLDILOCKS QCA GENERATE COMPLEXITY

Figure 2 shows a sampling of dynamical QCA outcomes. Although rule T_1 has been explored experimentally and rule T_{14} has been explored theoretically [38], only the Goldilocks rule T_6 displays nonequilibrating complexity at late times, visible in robust dynamical patterns. Complexity is produced by such Goldilocks rules for diverse initial states, activation unitaries, and time-evolution schemes. Conversely, rule T_{13} activates site j if (i) $|1\rangle$ appears as a left neighbor or (ii) zero or two neighbors occupy $|1\rangle$'s. T_{13} quickly equilibrates in almost all cases.

Figure 2(g)-(j) concern analog quantum computation and five-site blocks. Rule F_4 is a Goldilocks rule. It activates a site whose neighbors contain two $|1\rangle$'s but not zero, one, three, or four. The initial condition $|\ldots 000\,101\,000\ldots\rangle$ generates a *quantum entangled breather*, which parallels the breather of discrete nonlinear wave theory [39]. In contrast, the non-Goldilocks rule F_{26} rapidly destroys the state's structure.

The Goldilocks rules T_6 and F_4 exhibit late-time dynamical features. These features appear in the expectation value $\langle \hat{\sigma}_j^z \rangle$ (top row of Fig. 2) and the second-order Rényi entropy (bottom row). The non-Goldilocks rules exhibit no such persistent features. How can we quantify this lack of persistence? What is complexity?

Figure 3 quantifies complexity with the quantum mutual information, which generalizes a measure used throughout classical complexity theory. Complex networks can be imposed on quantum systems, such as networked NISQ (noisy intermediate-scale quantum) computers and in a quantum-Internet [40]. Yet complex networks can also emerge from a quantum state generated by noncomplex systems or models. This emergence has been demonstrated with the Ising and Bose-Hubbard models near quantum critical points [41, 42].

Figure 3(a) shows mutual-information networks for various states. We compare states produced by QCA with well-known examples: random ($|R\rangle$) [16], GHZ ($|G\rangle$), W ($|W\rangle$), and cluster ($|C\rangle$) states. The cluster state is defined in terms of a 1×19 lattice and a phase angle $\upsilon = \pi/4$ (see Section V for the definition). The Goldilocks rule T_6 has a visibly unusual network. Figure 3(b)-(c) show the time dependence of the network-averaged clustering ($\mathcal{C}$) and disparity ($\mathcal{Y}$). These measures (also defined in Section V) quantify complexity near
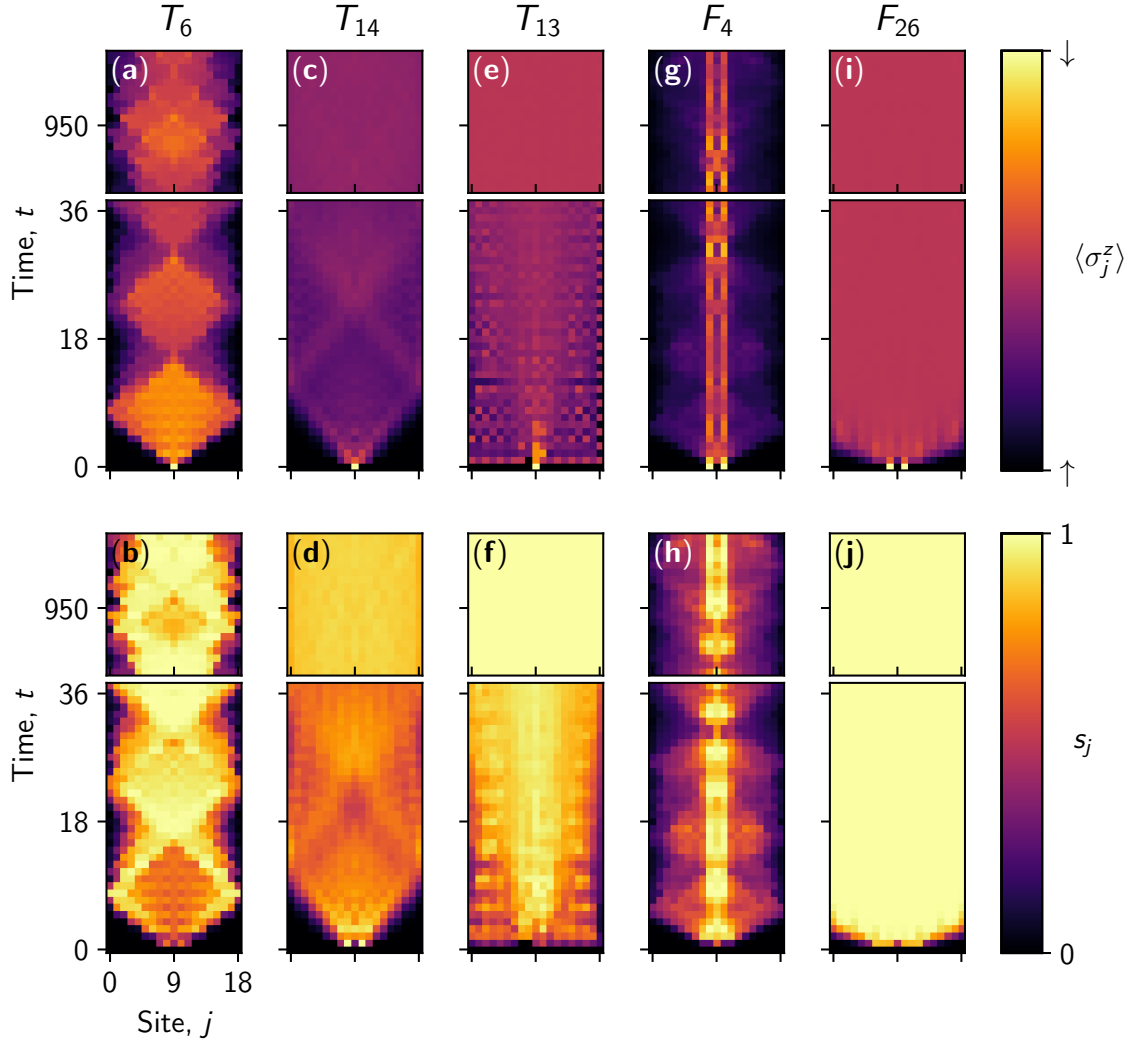
FIG. 2. Entangled QCA create diverse dynamical behaviors. For (a)-(f), an $L=19$-site chain was initialized with one $|1\rangle$ centered in $|0\rangle$'s, then evolved in discrete time. The rule-T_6 (a) spin and (b) entropy dynamics show patterns that resist equilibration for long times, as shown in each panel's upper block. (d) Under rule T_{14}, the spin dynamics rapidly equilibrate. (d) The entropy exhibits persistent patterns on a lower-entropy background. (e)-(f) In contrast, the rule-T_{13} dynamics rapidly equilibrate to a high-entropy state. For (g)-(j), we extend QCA to 5-site rules, initialize to $|101\rangle$, and evolve in continuous time. (g)-(h) The Goldilocks rule F_4 generates a quantum generalization of the blinker in Fig. 1(a), a *quantum entangled breather*. (i)-(j) In contrast, rule F_{26} promotes rapid equilibration to a high-entropy state.

quantum critical points. Solid curves show an activation phase angle of $v = 0$. Dashed curves show $v = \pi/2$, for T_{14}; other rules' features do not depend qualitatively on v. We studied many other complexity measures, including degree and path length [3]. Two measures suffice to illustrate that only rule T_6 consistently maintains more complexity: First, a large clustering often signals complexity [3]. The clustering remains large despite network growth only under the Goldilocks rule T_6 [Fig. 3(d)]. In fact, the network-and-time-averaged T_6 clustering grows with the network. Second, disparity fluctuations, while studied less commonly, signal a lack of equilibration. In Fig. 3(e), the disparity fluctuates the most under T_6.

Figure 3(f) shows the time-averaged clustering vs. the

central bond entropy, $s_{L/2}^{\text{bond}}$, for various initial conditions. T_6 generates complexity similarly to, but higher bond entropy than, the cluster state. The random state has a large bond entropy, low average clustering, and low average disparity, like the most non-Goldilocks rule, T_{13}.

Figure 3(g) shows how various initial conditions lead to states whose average disparity contrasts with well-known quantum states'. The GHZ and W states have high clusterings, low disparities, and low bond entropies. A high bond entropy can signal volume-law entanglement and chaos; and a low bond entropy, area-law entanglement and integrability. Goldilocks rules create new kinds of states, which are highly entangled (with bond entropies larger than the W and GHZ states') and highly complex
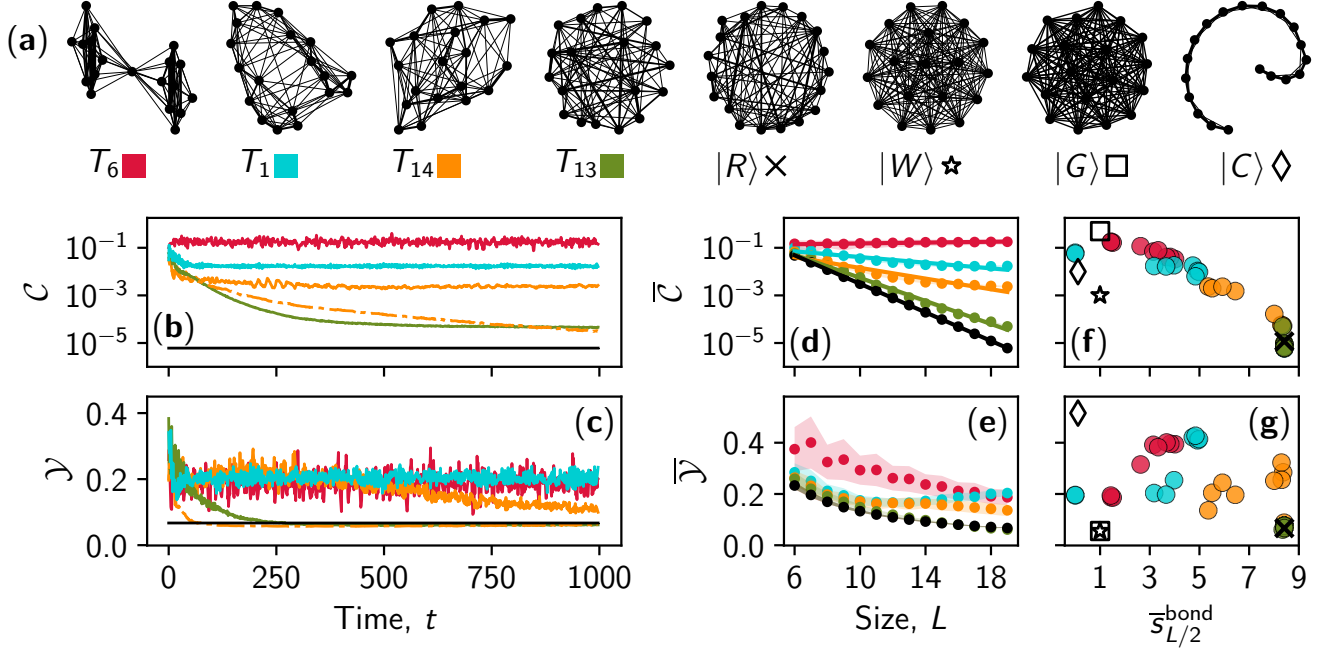
FIG. 3. (a) Four QCA were initialized with a central $|1\rangle$ centered in $|0\rangle$'s, then evolved for 500 time steps. The QCA complex networks (left-hand side) contrast with four well-known entangled states' networks (right-hand side). The networks' labels provide a legend for the panels below. (b)-(c) Clustering and disparity, well-known complex-network measures [3], averaged over the networks, vs. time. Solid lines result from an activation phase-gate angle $\upsilon = 0$. Dashed lines result from $\upsilon = \pi/2$ for T_{14}; the other rules' behaviors depend on υ negligibly. Under the Goldilocks rule T_6, the clustering remains high. The disparity oscillates rapidly, evidencing a lack of equilibration. In contrast, non-Goldilocks rules' clusterings decrease, and the disparities oscillate less. (d)-(e) Clustering and disparity, averaged over the network and time, vs. system size. Solid lines show exponential fits. Clustering tends to decrease exponentially with L, except for rule T_6, whose clustering increases. Disparity, too, tends to decrease, but at size-dependent rates (the rule-T_1 slope even changes sign). Each colored band depicts one standard deviation. Only T_6 generates fluctuations larger than the data points. Black lines in (b)-(c), and black data points in (d)-(e), follow from initializing the system in $|R\rangle$ and evolving with one of the four QCA, then averaging over the QCA. (f)-(g) Time-averaged clustering and disparity vs. central-bond entropy for various initial conditions (one or a few $|1\rangle$'s). QCA generate complexity only when initialized in low-enough-entropy states.

(exhibiting high disparity fluctuations and clustering).

Complexity is signaled by the convergence of several lines of evidence [3]. We emphasize high disparity fluctuations and clustering, together with entropy fluctuations (discussed below). Overall, Fig. 3 shows that the Goldilocks rule T_6 stands out from other rules and from well-known quantum states. For small-enough systems, T_1 presents a borderline case.

QCA defy the chaos/integrability classification scheme based on entanglement spectra, shown in Fig. 4(a) and detailed in Section V. Figure 4(b) shows the bond entropy's time derivative, $\Delta s_{L/2}^{\text{bond}}$. The derivative remains an order of magnitude higher for rule T_6 than for the other rules. This largeness signals complexity alternatively to network properties [45]. Dark lines show a moving average over L time steps. Faint lines, showing unaveraged data sampled every L time steps, illustrate fluctuations. The random background (gray shading) extends between the mean $\pm$ the standard deviation of data from initializing with $|R\rangle$, then evolving under different rules in different trials.

The Page curve distinguishes area-law and volume-law entanglement. Let $\ell = 0, 1, \ldots, L - 2$ denote the bipartitionings of the lattice. The bond entropies for all the bipartitionings, s_ℓ^{bond}, form the Page curve. Figure 4(c) shows the Page curves for QCA-generated states. The T_6 curve, being lowest, suggests an area law the most. If the initial state contains exactly one $|1\rangle$, the Page curve fits the scrambled-state ansatz in [47]. Many initial $|1\rangle$'s lead to T_6 Page curves (not shown) that disobey a volume law and deviate significantly from the scrambled-state prediction. Similarly, many-body scars—nonequilibrating features discovered under T_1 evolution (the PXP model)— are theorized to arise from a few area-law energy eigenstates states amidst a volume-law sea. Yet observing many-body scars requires special initial conditions. Fine-tuning is not necessary for resistance to equilibration under Goldilocks rules: Complexity emerges for diverse initializations, activation operators, time-evolution schemes, and update orderings.

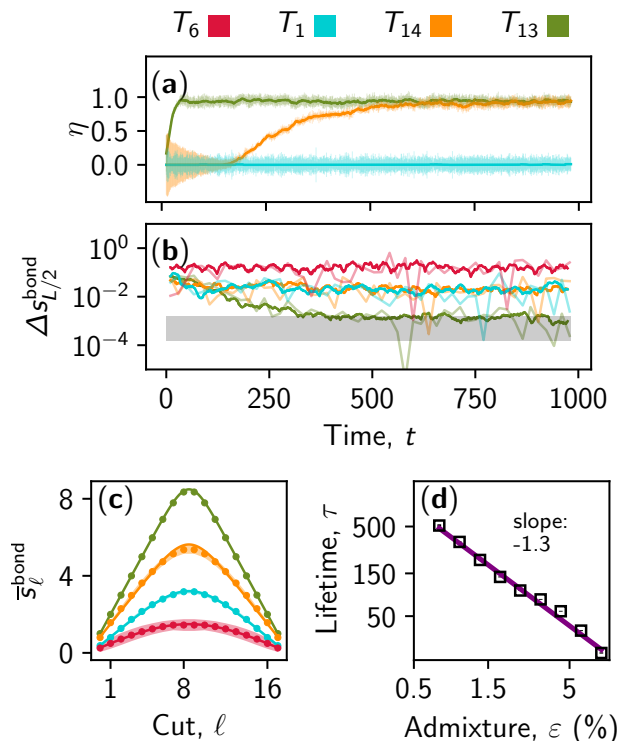This complexity survives perturbations and noise. Figure 4(d) demonstrates robustness of the quantum en-

FIG. 4. Dynamical many-body features distinguish
Goldilocks QCA. (a) The Brody parameter η interpolates
between integrable systems' Poisson statistics ($\eta = 0$) and
chaotic systems' Wigner-Dyson statistics ($\eta = 1$). We cal-
culate η from entanglement spectra [43]. η grows to chaotic
values under rules T_{13} and T_{14}, remaining Poissonian under
T_1. The T_6 η defies the paradigm and so is not plotted: Many
eigenvalues ≈ 0. Bars represent the error prescribed by the
η-extraction procedure. (b) Entropy fluctuations distinguish
integrable from chaotic systems alternatively to the Brody
parameter [44] and suggest complexity [45]. The fluctuations
are 1-3 orders of magnitude larger for T_6 than for T_1, T_{14}, and
the random background (gray shading). (c) The Page curve
distinguishes between area and volume laws, characteristic
of integrable and chaotic many-body models [46, 47]. The
T_{13} curve, bending far upward, suggests a volume law; T_6
and T_1 come closer to achieving area laws. The T_{14} curve
deviates from the scrambled-state ansatz. Dots represent
time-averaged Page curves; solid curves, the best fits to the
scrambled-state ansatz; and shaded regions, time fluctuations.
(A-C) report on $L = 19$ sites initialized with one centered $|1\rangle$.
(d) The continuous-time rule F_4 produces robust quantum
entangled breathers [Fig. 2(g)-(h)]. F_4 was perturbed with a
non-Goldilocks rule, F_{26}, at strength ε. The breather's life-
time decays as a power law: $\tau \propto \varepsilon^{-1.3}$.

tangled breather generated with the Goldilocks rule F_4
[Fig. 2(g)-(h)]. We perturbed F_4 with the non-Goldilocks
rule F_{26}, with strength ε. The breather's lifetime, τ,
varies with ε as a slow power law. Quantum entangled
breathers survive also imperfect initializations and limi-
tations on entanglement (Schmidt truncation). Emergent
power laws, with features such as high clustering, dispar-
ity fluctuations, and entropy fluctuations, provide evi-

dence of complexity's emergence under Goldilocks rules.

IV. MODEL DETAILS

In this section, we present explicit formulae for the
T-type unitaries and the F-type Hamiltonians, as func-
tions of rule number. We then interrelate the two time-
evolution schemes by considering a three-site analog pro-
tocol. Our rule numbering is inspired by elementary-
cellular-automata rule numbering, so we first discuss
those classical models.

A. Classical Elementary Cellular Automata

A classical-ECA neighborhood consists of a central bit
and its two nearest neighbors. Classical ECA rules are
denoted by C_R. The rule number R encodes the local
transition function, which prescribes a bit's next state
for any possible neighborhood configuration. A bit has
two possible values (0 or 1), and ECA neighborhoods
consist of three sites. Hence a neighborhood can occupy
$2^3 = 8$ configurations, which lead to $2^{2^3} = 256$ rules.

The system is evolved through one time step as fol-
lows. First, a copy of the bit string is produced. Each
site's neighborhood is read off of the copy and is inputted
into the local transition function. The function's output
dictates a site's next state, which is written to the origi-
nal bit string. The copying allows all sites to be updated
independently, simultaneously.

The rule encoding works as follows. Given C_R, ex-
pand R into 8 binary digits, including leading zeroes:
$R = \sum_{n=0}^{7} c_n 2^n$. The index n enumerates the neigh-
borhood configurations when expressed as a sequence of
three binary digits: $n = \sum_{m=0}^{2} k_m 2^k$. The binary ex-
pansion of n is the equivalence of the base-10 number n
and the base-2 number $k_2 k_1 k_0$. The binary expansion
$n \equiv k_2 k_1 k_0$ encodes the neighborhood's state. In the bi-
nary expansion of R, the coefficients $c_n \in \{0, 1\}$ dictate
the next state of the neighborhood's central site. Fig-
ure 5 shows the update table for rules $R = 30$, 60, and
110. Also depicted are the time evolutions of a 1 centered
in 0s.

B. Entangled quantum cellular automata

Entangled QCA can be realized with 1D chains of L
qubits, or sites. Dynamics are governed by a QCA Hamil-
tonian (equivalently, by analog quantum computation,
or a quantum simulator) or by a quantum circuit (by a
digital quantum computer). Each time-evolution scheme
specifies how a site j updates conditionally on the state
of the site's neighbors. The neighbors within a radius r
of site j form a set denoted by Ω_j. (Ω_j does not include
j.) Some of our QCA have three-site neighborhoods, of
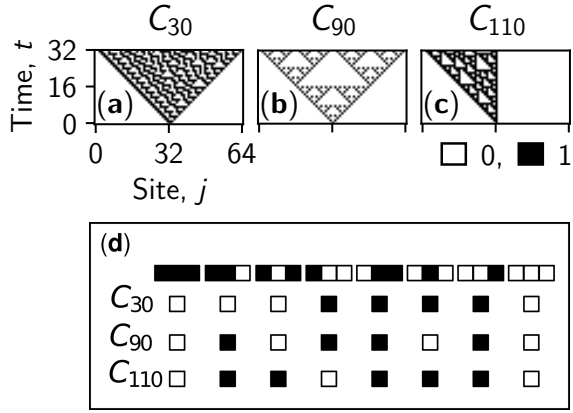a central site j and its nearest neighbors. Some of our

FIG. 5. (a-c) Classical-elementary-cellular-automata (ECA) evolutions of a 1 centered in 0s. (d) Rule tables for C_{30}, which generates pseudorandom numbers; C_{60}, which generates a fractal structure; and C_{110}, which is Turing-complete (capable of simulating any computer program).

QCA have five-site neighborhoods, of site j and its nearest neighbors and next-nearest neighbors. The QCA rule number encodes the coupling's form, i.e., conditions on the neighbors which activate site j.

Neither of our update schemes (discrete-time or continuous-time) decomposes into a component governed by left-hand neighbors and a component governed by right-hand neighbors. Our schemes' bidirectionality contrasts with the structures of most many-body Hamiltonians in the literature and solved on quantum computers. Examples include the Hubbard, Ising, and Heisenberg models; the PXP model constitutes an exception [7]. Nevertheless, our scheme can be realized experimentally, as we show later.

Our QCA's definitions differ from ECA's definitions in four ways: (i) Sites are evolved in place, rather than via copying. How the lattice evolves, therefore, depends on the order in which sites update. Complexity outcomes, we find, do not depend on how site updates are ordered. For instance, site 0 can update, followed by site, 1, and so on: ($\{0\}, \{1\}, \ldots$). Alternatively, the even sites can update simultaneously, followed by the odd sites: ($\{0, 2, \ldots\}, \{1, 3, \ldots\}, \{0, 2, \ldots\}, \ldots$). Other options exist, e.g., ($\{0, 3, 6, \ldots\}, \{1, 4, 7, \ldots\}, \{2, 5, 8, \ldots\}, \ldots$). We therefore present about only the second scheme, even-odd ordering. (ii) Rules dictate how a site evolves, not the state to which the site evolves. (iii) In QCA, how site j evolves depends only on the site's neighbors, not on the site itself. (iv) An ECA neighborhood consists of three sites. We present QCA that have three-site neighborhoods and QCA that have five-site neighborhoods.

Our QCA models' rule numbering is defined in terms of the neighborhood size, the rule number R, and whether the rule numbering is totalistic. The three-site-neighborhood rules are labeled as T_R; the five-site-neighborhood rules are labeled as F_R.

Under a totalistic rule, whether the activation operator transforms a neighborhood's central site depends only on the total number of neighboring $|1\rangle$'s. If the neighborhood consists of three sites, zero, one, or two neighbors can be in the state $|1\rangle$. Hence $2^3 = 8$ totalistic three-site rules exist. They form a subset of the general $2^{2^2} = 16$ T_R rules. Similarly, $2^5 = 32$ F_R rules exist. They form a subset of the $2^{2^4} = 65536$ general five-site rules. The number of rules grows combinatorially with the neighborhood's size. Under a Goldilocks rule, whether a site updates depends on a neighborhood's total value, satisfying the "not too many and not too few" tradeoff common in complexity theory [36]. If we did not invoke totalistic labeling of five-site-neighborhood rules, rule F_4 would have rule number $R = 5736$.

To specify a QCA model, one must specify, in addition to a rule number R, a time-evolution scheme (digital or analog) and an activation operator. Equations (1) and (2) of Section II formalize these requirements. We narrow down the options to two illustrative choices: The T-type simulations discussed involve digital evolution with a Hadamard-and-phase-gate activation. The F-type simulations discussed involve analog evolution and a $\hat{\sigma}^x$ activation. (Below, we present the T-rule unitaries' and F-rule Hamiltonians' forms.) Yet analog and digital evolutions can be performed with any neighborhood size. We discuss analog T_R rules (i) when interrelating the digital and analog evolution schemes and (ii) when proposing physical implementations. Digital evolution of rules with larger neighborhoods can be generalized as follows: Recall that r denotes the radius of neighbors that determine whether a central site updates. Instead of updating even sites, then odd sites, we run $r + 1$ layers of a quantum circuit. Layer $k \in \{0, 1, \ldots, r\}$ updates site j if $j \mod (r + 1) = k$.

C. T-type simulations

Rules T_R denote digital simulations of the 3-site-neighborhood rules. To expose such a rule's dynamics, convert R from base-10 into four base-2 bits (including leading zeroes). The leftmost bit should be the most significant; and the rightmost bit, the least significant: $R = c_{11}2^3 + c_{10}2^2 + c_{01}2^1 + c_{00}2^0 = \sum_{m,n=0}^{1} c_{mn} 2^{2m+n}$. The m specifies the left-hand neighbor's value; and n specifies the right-hand neighbor's value. $c_{mn} \in \{0, 1\}$ specifies whether the central bit evolves under a single-qubit unitary $\hat{V}$ ($c_{mn} = 1$) or under the identity $\hat{\mathbb{1}}$ ($c_{mn} = 0$), given the neighbors' values. More concretely, the three-site update unitary has the form

$$\hat{U}_j(\hat{V}) = \sum_{m,n=0}^{1} \hat{P}_{j-1}^{(m)} \hat{V}_j^{c_{mn}} \hat{P}_{j+1}^{(n)}. \qquad (3)$$

The superscript on $\hat{V}_j$ denotes a matrix power. We update the lattice by applying $\hat{U}_j(V)$ to each 3-site neigh-

borhood centered on site j, for every j. Even-j neighborhoods update first; and odd-j neighborhoods, second. Each boundary qubit is fixed to $|0\rangle$. We explored alternative boundary conditions, including periodic boundary conditions and boundaries fixed to $|1\rangle$'s. The complexity outcomes are similar.

The local update unitary $\hat{V}_j$ is the product of the Hadamard and phase gates familiar from quantum computing:

$$\hat{V}_j \equiv \hat{V}_j(\upsilon) = \hat{U}_{\mathrm{H}}\hat{U}_{\mathrm{P}}(\upsilon) = \frac{1}{\sqrt{2}} \begin{pmatrix} 1 & e^{i\upsilon} \\ 1 & -e^{i\upsilon} \end{pmatrix}. \qquad (4)$$

The Hadamard gate rotates the Bloch sphere's north pole to the x-axis. A phase gate of $\upsilon = \pi/2$ rotates the x-axis into the y-axis. These gates can rotate a qubit state to any point on the Bloch sphere. In most of the simulations investigated here, $\upsilon = 0$; the dynamics is restricted to the xz-plane. Behaviors are mostly robust with respect to changes in υ. T_{14} forms an exception: Nonzero υ values strongly suppress entropy fluctuations.

D. F-type simulations

F_R denotes analog simulations of five-site totalistic rules with a Hermitian activation operator $\hat{h}_j = \hat{\sigma}_j^x$. The value of R dictates the form of the many-body Hamiltonian $\hat{H} = \sum_j \hat{H}_j$. We expand R into 5 digits of binary: $R = \sum_{q=0}^{4} c_q 2^q$. Site j evolves conditionally on its neighbors:

$$\hat{H}_j = \hat{\sigma}_j^x \sum_{q=0}^{4} c_q \hat{\mathcal{N}}_j^{(q)}. \qquad (5)$$

$\hat{\mathcal{N}}_j^{(q)}$ denotes the projector onto the q-totalistic subspace, in which exactly q neighbors are in $|1\rangle$'s:

$$\hat{\mathcal{N}}_j^{(q)} = \sum_{\mathrm{perm}(K_q)} \hat{P}_{j-2}^{(K_q[0])} \hat{P}_{j-1}^{(K_q[1])} \hat{P}_{j+1}^{(K_q[2])} \hat{P}_{j+2}^{(K_q[3])}. \qquad (6)$$

K_q represents a sequence of q ones followed by $4 - q$ zeroes. $K_q[i] \in \{0, 1\}$ denotes the sequence's i^{th} element. The sum is over the $\binom{4}{q}$ permutations of the bits in K_q. Qubits near the boundary do not have a complete set of neighbors. Any missing neighbors are fixed to $|0\rangle$'s. Other boundary conditions yielded similar results.

We illustrate continuous-time evolution with five-site neighborhoods, the smallest we found to produce quantum entangled breathers. These emergent features suggest complexity greater than the three-site scheme's. The three-site analog scheme, too, generates complexity but provides no information beyond the discrete-time scheme. Likewise, we explored diverse Hermitian activation operators $\hat{h}_j$. They generate complexity when coupled with a nontrivial $\hat{h}_j$ and initial state. By "nontrivial," we mean that the initial state is not an eigenstate of the Hamiltonian. In trivial cases, the evolution only introduces a global phase.

E. Relation between analog and digital time-evolution schemes

We will prove that evolution under analog three-site QCA is equivalent to evolution under the digital three-site QCA, T_R. [48] Consider the radius-1 analog QCA T_R, with rule number $R = \sum_{m,n} c_{mn} 2^{2m+n}$. According to Eq. (2), the three-site Hamiltonian has the form

$$\hat{H}_j = \sum_{m,n=0}^{1} c_{mn} \hat{P}_{j-1}^{(m)} \hat{\sigma}_j^x \hat{P}_{j+1}^{(n)}. \qquad (7)$$

The state vector is evolved for a time δt by the propagator $\hat{U} = \exp(-i\delta t \hat{H})$. For all j and k such that $|k - j| \neq 1$, $[\hat{H}_j, \hat{H}_k] = 0$. Hence the propagator factorizes into even and odd parts at order δt^2: $\hat{U} \approx \left(\Pi_{j \in \{1,3,5,\dots\}} \hat{U}_j\right) \cdot \left(\Pi_{j \in \{0,2,4,\dots\}} \hat{U}_j\right)$. The local propagator has been defined as $\hat{U}_j = \exp(-i\delta t \hat{H}_j)$. This $\hat{U}$ is equivalent to the circuit that runs the digital T_R simulations, up to the unitary activation operator $\hat{V}_j$.

Now, we relate the discrete-time scheme's $\hat{V}_j$ to the continuous-time scheme's $\hat{h}_j = \hat{\sigma}^x$. We expand the local propagator as $\hat{U}_j = \hat{\mathbb{1}} - i\delta t \hat{H}_j - \delta t^2 \hat{H}_j^2/2! + i\delta t^3 \hat{H}_j^3/3! + \dots$ The projectors are orthogonal, $\hat{P}_j^{(m)} \hat{P}_j^{(n)} = \delta_{mn} \hat{P}_j^{(m)}$, and the Pauli operators square to the identity: $(\hat{\sigma}^x)^2 = \hat{\mathbb{1}}$. Therefore, powers of the Hamiltonian can be expressed as $\hat{H}_j^{2k} = \sum_{m,n} c_{mn} \hat{P}_{j-1}^{(m)} \hat{\mathbb{1}} \hat{P}_{j+1}^{(n)}$ and $\hat{H}_j^{2k+1} = \hat{H}_j$ for $k = 1, 2, \dots$ Hence the matrix exponential simplifies to

$$\hat{U}_j = \sum_{m,n=0}^{1} \hat{P}_{j-1}^{(m)} \left[(1 - c_{mn}) \hat{\mathbb{1}} + c_{mn} \exp(i\delta t \hat{\sigma}_j^x)\right] \hat{P}_{j+1}^{(n)}$$

$$= \sum_{m,n=0}^{1} \hat{P}_{j-1}^{(m)} \exp(i\delta t \hat{\sigma}_j^x)^{c_{mn}} \hat{P}_{j+1}^{(n)}.$$

The last line has the form of the three-site update unitary in Eq. (3). The parallel suggests an activation unitary $\exp(i\delta t \hat{\sigma}^x)$.

V. METHODS AND DEFINITIONS

Throughout this work, we use various numerical and statistical methods, quantifiers of dynamics, and complex networks. This section details those methods and definitions.

A. Well-known quantum states

Figure 3 involves four well-known quantum states: the GHZ state, the W state, a random state, and a cluster state. The GHZ state is defined as $|G\rangle = 2^{-1/2}(|00\dots0\rangle + |11\dots1\rangle)$; and the W state, as $|W\rangle =$

$2^{-L/2}(|100\ldots0\rangle + |010\ldots0\rangle + \cdots + |00\ldots01\rangle)$). We define the random state as $|R\rangle = C\sum_n \xi_n |n\rangle$. The normalization constant is denoted by C. The ξ_n are random complex numbers with real and imaginary parts drawn independently from a flat distribution over $[0,1)$. The $|n\rangle$ are the 2^L computational-basis elements for an L-qubit system.

A cluster state is a quantum state defined by a regular graph $G(V,E)$. The set of vertices, or nodes, is denoted by V; and the set of edges, or links, by E. The number of nodes equals the number of qubits in the cluster state. We focus on planar rectangular grids of L vertices. No matter the graph, the cluster state is constructed in two steps. First, each qubit is initialized in $|0\rangle$ and transformed, by a Hadamard gate, to $2^{-1/2}(|0\rangle + |1\rangle)$. Second, a controlled-phase gate

$$\hat{C}_{\text{phase}}(v) = \begin{pmatrix} 1 & 0 & 0 & 0 \\ 0 & 1 & 0 & 0 \\ 0 & 0 & 1 & 0 \\ 0 & 0 & 0 & e^{iv} \end{pmatrix} \quad (8)$$

acts on every pair of nodes in the edge list E. The second step tends to generate entanglement along the graph's links.

B. Local expectation values

Let $\hat{\mathcal{O}}_j$ denote an observable of qubit j. The observable has a dynamical expectation value of $\left\langle \hat{\mathcal{O}}_j \right\rangle(t) = \text{Tr}\left(\hat{\rho}_j(t)\hat{\mathcal{O}}\right)$, where $\hat{\rho}_j(t)$ denotes the site-j reduced density matrix, calculated by partially tracing over the whole-system density matrix $\hat{\rho}(t) = |\psi(t)\rangle\langle\psi(t)|$, i.e., $\hat{\rho}_j(t) = \text{Tr}_{k\neq j}\hat{\rho}(t)$.

C. Entropy

Let $\mathcal{A}$ denote a subsystem in the state $\hat{\rho}_{\mathcal{A}}$. The *order-α Rényi entropy* is defined as

$$s_{\mathcal{A}}^{(\alpha)} = \frac{1}{1-\alpha}\log_2\left[\text{Tr}(\hat{\rho}_{\mathcal{A}}^{\alpha})\right] \quad (9)$$

for $\alpha \in [0,1) \cup (1,\infty)$. In the limit as $\alpha \to 1$, the Rényi entropy becomes the von Neumann entropy:

$$s_{\mathcal{A}}^{(1)} = -\text{Tr}\left(\hat{\rho}_{\mathcal{A}}\log_2\hat{\rho}_{\mathcal{A}}\right) = -\sum_{i=0}^{\dim(\mathcal{A})}\lambda_i\log_2(\lambda_i). \quad (10)$$

The sum runs over the eigenvalues $\{\lambda_i\}$ of $\hat{\rho}_{\mathcal{A}}$. The set $\{\lambda_i\}$ of eigenvalues is called the *entanglement spectrum* of subsystem $\mathcal{A}$.

We distinguish three Rényi entropies. First, the *local entropy* $s_j^{(\alpha)}$ is the jth site's entropy. Second, the *two-point entropy*, $s_{j,k}^{(\alpha)}$ for $j \neq k$, is of a pair of sites. Third,

consider cutting the lattice between sites ℓ and $\ell+1$. The smaller subsystem has an entropy $s_\ell^{\text{bond},(\alpha)}$ called the *bipartition bond entropy*. The central cut's bond entropy is denoted by $s_{L/2}^{\text{bond},(\alpha)}$. If the system has an odd number L of sites, the central bond lies between sites $(L-1)/2$ and $(L+1)/2$.

The $\alpha = 2$ Rényi entropy is routinely measured experimentally [49]. Therefore, Section III focused on $\alpha = 2$, where we dropped the superscript (2) to simplify notation.

Temporal fluctuations in entropy are captured with the absolute value of a second-order central finite difference. [50] In discrete-time simulations, the time step has unit length. Hence the fluctuation at time step t_i is

$$\Delta s_{\mathcal{A}}^{(\alpha)}(t_i) = \frac{1}{2}\left|s_{\mathcal{A}}^{(\alpha)}(t_{i+1}) - s_{\mathcal{A}}^{(\alpha)}(t_{i-1})\right|. \quad (11)$$

For simplicity, we suppress the time dependence in the left-hand side's notation. The absolute value highlights the fluctuations' magnitudes, suppressing the signs.

The set of all the bond entropies $s_\ell^{\text{bond},(\alpha)}$, for $\ell = 0$ to $L-2$, is called a *Page curve*. Consider averaging the $\alpha = 2$ Page curve over the last half of the time evolution.

We denote with an overbar the late-time average of any length-T time-series Q that includes only times greater than $t_0 \sim T/2$: $\overline{Q}(t_i) = \sum_{t_i=t_0}^{T} Q(t_i)/(T-t_0)$. The average Page curve is fit with the ansatz [47]

$$\overline{s}_\ell^{\text{bond},(2)} = (\ell+1)\log_2(a) - \log_2\left(1 + a^{2(\ell+1)-L}\right) + \log_2(K). \quad (12)$$

a and $\log_2(K)$ denote free parameters. The first term in Eq. (12) represents volume-law entanglement growth with slope $\log_2(a)$. $a = 1$ signals an area law. When $\ell \in [0, L/2]$, the second term represents a deviation from the volume law. The deviation grows as the cut nears the lattice's center. The third term represents an offset to the volume law.

Figure 6(a) shows Eq. (12) for different a values. $\log_2(K)$ is fixed so that $\overline{s}_0^{\text{bond},(2)} = 0$. Nonintegrable systems are conjectured to have Page curves that tend towards Eq. (12); and integrable systems, to have Page curves that deviate. More information appears in [47], whose conventions deviate from two of ours: (i) Our definition of ℓ is shifted relative to theirs; hence the $\ell+1$ in Eq. (12). (ii) Our entropies' logarithms are base-2.

D. Entanglement-spectrum statistics

Consider cutting the lattice down the center. Each subsystem's reduced state has eigenvalues λ_i, which form the entanglement spectrum [51]. We index the eigenvalues such that $\lambda_1 \leq \lambda_2 \leq \ldots$ How many spacings $\lambda_{i+1} - \lambda_i$ have size d? The density of size-d gaps forms a distribution that we fit to the *Brody ansatz* [52],

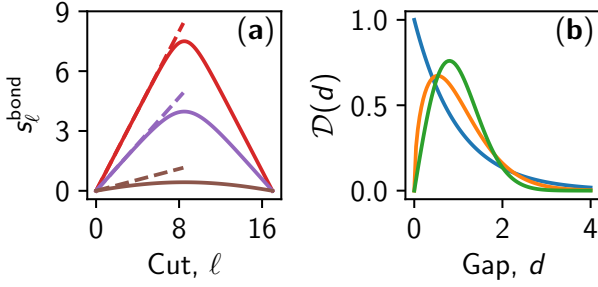$$\mathcal{D}(d) = \beta(\eta+1)d^\eta\exp(-\beta d^{\eta+1}). \quad (13)$$

FIG. 6. (a) The Page-curve ansatz (12), for $a = 2.0$ (red) 1.5 (purple), and 1.1 (brown). $\log_2(K)$ is fixed, for all curves, such that the minimum entropy vanishes. The dashed lines represent the corresponding volume law, the first term in Eq. (12). Integrability can cause a high-energy Hamiltonian eigenstate's Page curve to deviate from such a best fit [47]. (b) The Brody ansatz (13) for $\eta = 0.0$ (blue), 0.5 (orange), and 1.0 (green). Poisson ($\eta = 0$) statistics promote small gaps; Wigner-Dyson ($\eta = 1$) statistics promote eigenvalue repulsion. The gap d is normalized to have a unit average.

Γ denotes the gamma function, $\beta = \Gamma\left(\frac{\eta+2}{\eta+1}\right)^{\eta+1}$, and $\eta \in [0,1]$ is the *Brody parameter*. This ansatz interpolates between Poisson statistics ($\eta = 0$), characteristic of integrable systems, and Wigner-Dyson ($\eta = 1$) statistics, characteristics of nonintegrable systems [Fig. 6(b)].

The ansatz is derived under the assumption that d averages to one. This condition is often enforced via a spectral unfolding procedure. We use the polynomial method [53]: We remove all $\lambda_i < 10^{-10}$, then the 10 smallest and 10 largest λ_i values. This clipping is a standard preprocessing tool, eliminating outliers and $\lambda_i \approx 0$. Next, we fit a generic ninth-order polynomial $f(x) = \sum_{n=0}^{9} b_n x^n$ to the set of ordered pairs (λ_i, i). The unfolded spectrum is defined by the dimensionless variable $\lambda_i' = f(\lambda_i)$. The rescaled spacings d_i are calculated from the λ_i'. This procedure ensures that d_i averages to 1 because $\lambda_i' \approx i$, so every $d_i \approx 1$.

Consider initializing the lattice with a $|1\rangle$ centered in $|0\rangle$'s. Evolving with rule T_6 leads to only 11 values of $\lambda_i > 10^{-10}$. A small sample size dooms any statistical measure, so we omit T_6 from Fig. 3(a). Entropy fluctuations distinguish integrability from nonintegrability alternatively, as we showed in work on the quantum ratchet's many-body chaos [44].

E. Mutual information

The mutual information quantifies networks' complexity. A *complex network* is network, or graph—a collection of nodes, or vertices, and links, or edges—that is neither regular nor random [3]. For example, completely connected graphs and Erdős-Rényi graphs are not complex networks.

The order-α quantum Rényi mutual information between sites j and $k \neq j$ is

$$M_{jk}^{(\alpha)} = \frac{1}{2}\left| s_j^{(\alpha)} + s_k^{(\alpha)} - s_{jk}^{(\alpha)} \right| . \qquad (14)$$

The $1/2$ is unconventional but normalizes the mutual information such that $0 \leq M_{jk}^{(\alpha)} \leq 1$. We define $M_{jj}^{(\alpha)} = 0$ and interpret $M_{jk}^{(\alpha)}$ as the adjacency matrix of a weighted, undirected graph that lacks self-connections. The absolute value in Eq. (14) is necessary only for $\alpha > 1$.

For $\alpha = 1$, the mutual information is positive-definite. It has the physical interpretation of an upper bound on every two-point correlator [54]. Hence a nonzero $M_{jk}^{(1)}$ reflects two-point correlations. Yet the order-2 Rényi entropy is routinely measured in experiments, so we focus on $M_{jk}^{(2)}$. The complexity outcomes for $\alpha = 1, 2$ are qualitatively similar, as in the context of quantum phase transitions [42]. To simplify notation, we drop the (α) superscript in Section III. An adjacency matrix can be defined alternatively in terms of two-point correlators, but they capture complexity less than mutual information does [42].

F. Network measures

Network measures are functions of an adjacency matrix; they quantify the corresponding graph's connectivity. We evaluate two network measures on mutual-information adjacency matrices: the clustering coefficient and the disparity. They capture complexity in the context of quantum phase transitions near quantum critical points [41, 42].

First, the *clustering coefficient* $\mathcal{C}$ quantifies local, small-scale community structure. Clustering is a key feature of social and biological networks. It quantifies transitivity: Suppose that node A connects to node B, which connects to node C. A likely connects to C if the network has high clustering. The clustering coefficient equals the number of connected triangles, divided by the number of possible connected triangles. If M denotes an $L \times L$ adjacency matrix,

$$\mathcal{C}(M) = \frac{\text{Tr}\left(M^3\right)}{\sum_{\substack{j,k=0 \\ j \neq k}}^{L-1} [M^2]_{jk}} . \qquad (15)$$

Clustering is known to be high for complex networks, e.g., Watts-Strogatz networks [3].

The second complex-network measure, *disparity*, quantifies how much a network resembles a backbone. The disparity is defined as

$$\mathcal{Y}(M) = \frac{1}{L} \sum_{j=0}^{L-1} \frac{\sum_{k=0}^{L-1} (M_{jk})^2}{\left(\sum_{k=0}^{L-1} M_{jk}\right)^2} . \qquad (16)$$

Two examples illuminate this definition. First, consider a uniform network: $M_{jk} = a$, except along the diagonal, where $M_{jj} = 0$. This network has a disparity of

$\mathcal{Y} = 1/(L-1)$. Second, a 1D chain has an adjacency matrix of $M_{jk} = a(\delta_{j(k+1)} + \delta_{j(k-1)})$ and so a disparity of $\mathcal{Y} = (L+2)/(2L)$. If $L = 2$, the two networks describe the same graph, so each has $\mathcal{Y} = 1$. As L increases, the fully connected network's disparity approaches 0, while the 1D chain's approaches 0.5. Figure 3(b)-(g) show average clusterings and disparities for various quantum states. Fluctuations in the disparity [3] indicate a lack of equilibration under the Goldilocks rule T_6: The network repeatedly forms and breaks a backbone.

G. Quantum-entangled-breather lifetime

Rule F_4 generates a quantum entangled breather [Fig. 2(g)-(h)]. The system is initialized with two centered $|1\rangle$'s separated by a $|0\rangle$. Left unperturbed, the state oscillates indefinitely. Figure 4(d) shows how the breather decays under perturbations of three types.

First, we add the rule-F_{26} Hamiltonian, scaled by a positive $\epsilon \ll 1$, to the F_4 Hamiltonian. Rule 26 activates a site whenever its neighbors contain at least one $|1\rangle$. Second, we perturb the QCA via Schmidt truncation: We evolve the system with a matrix-product-state approximation. The Hilbert space's effective dimensionality is reduced from $\chi = 2^{L/2}$ until the breather becomes unstable. This truncation time-adaptively caps the amount of entanglement in the state [55]. Third, imperfect initialization affects τ. The initial $|1\rangle$'s are replaced with copies of $\epsilon e^{i\phi} |0\rangle + \sqrt{1 - \epsilon^2} |1\rangle$. The perturbation's strength is quantified by the positive $\epsilon \ll 1$; ϕ turns out not to affect the breather's stability. Consider the qubit one site leftward of the center, the qubit at site $j = \lfloor L/2 \rfloor - 1$ (since $j = 0, 1, \ldots, L - 1$). This qubit's projection onto $|1\rangle$ is fitted with

$$\left\langle \hat{P}^{(1)}_{\lfloor L/2 \rfloor - 1} \right\rangle (t) = \frac{1}{2} \left[1 - \left\langle \hat{\sigma}^z_{\lfloor L/2 \rfloor - 1} \right\rangle (t) \right] = A + B e^{-t/\tau} . \tag{17}$$

From the fit, we extract the lifetime τ. Figure 7 illustrates the fitting procedure used to produce Fig. 4(d), run on $L = 17$ sites.

The quantum entangled breather is robust with respect to all three perturbations. The breather's lifetime depends on the Hamiltonian perturbation as a slow inverse power law: $\tau \propto \varepsilon^{-1.3}$. Under Schmidt truncation, the lifetime exhibits a sharp threshold at $\chi = 8\text{-}10$. Below the threshold, $\tau \propto \chi^{-7}$; above, τ exceeds the simulation time, $T = 1,000$. For imperfect initialization, we find stability for $\epsilon \leq 1/2$, independently of ϕ: The breather has an infinite lifetime. However, increasing ϵ decreases the visibility of the breather's oscillations between $|1\rangle$ and $|0\rangle$ [Fig. 2(g)].

H. Numerical and statistical methods

In simulations, quantities are rescaled such that $\hbar = 1$, and energies and times are dimensionless. We deviate
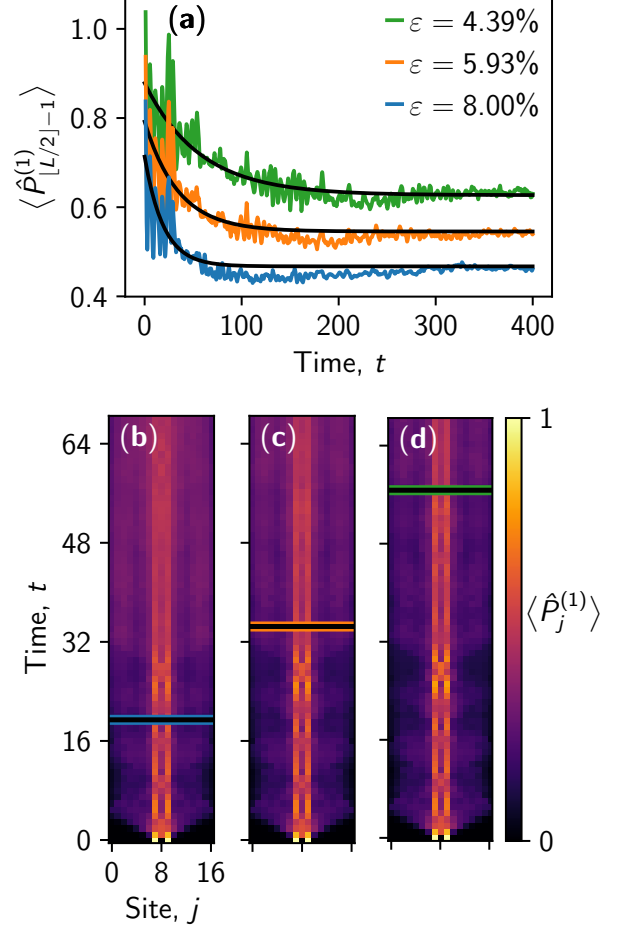

FIG. 7.   A quantum entangled breather's robustness. (a) The breather is generated by the Goldilocks rule F_4. We perturb F_4 with the non-Goldilocks rule F_{26} at strength ε. Black curves show the exponential fit of Eq. (17). Each curve is shifted by 0.1 from the curve below it, to ease visualization. (b)-(d) Space-time dependence of the average excitation density, defined through the projection of each site's state onto $|1\rangle$. The lifetime, defined as τ in Eq. (17), ends at double bars color-coded in accordance with (a).

from this convention only when discussing physical implementations of QCA. If multiple energy scales must be specified, time units are presented.

We have developed a custom QCA-simulation library, used to generate most of the data analyzed in this Report. The library simulates time evolution using optimized diagonalization code. Analog QCA propagators are represented exactly or are approximated to second or fourth order in the time-step length. We introduced the second-order approximation analytically when proving the equivalence of our analog and digital time evolutions. The analog scheme involved a Hamiltonian $\hat{H}$ that generated a unitary $\hat{U}$. $\hat{U}$ factorized into even and odd unitaries at order $(\delta t)^2$. The fourth-order approximation
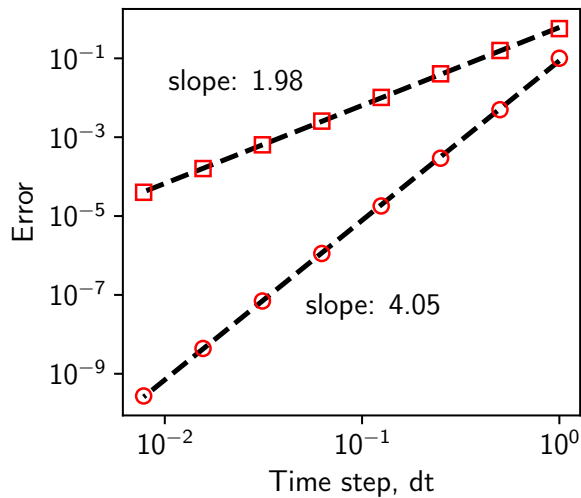
FIG. 8. Convergence of numerical time-evolution algorithm for order-2 routine (squares) and order-4 routine (circles). We initialized an $L=11$-site lattice to a random state $|R\rangle$, then simulated one time step of the analog rule T_6.

partially updates even-j sites, fully updates odd-j sites, then finishes updating even-j sites. By definition, the digital QCA are exact, to numerical precision.

We define the error as $1 - |\langle\tilde{\psi}|\psi\rangle|^2$. $|\psi\rangle$ denotes the state at the last time step of evolution by the full propagator. $|\tilde{\psi}\rangle$ denotes the analogous state after evolution by the approximate propagator. Figure 8 shows the error after one time step, plotted against the time step's length. The data exhibit the anticipated order-2 and order-4 scalings, as compared with the exact evolution.

We simulate F-type QCA using the OpenMPS library, which has been tested thoroughly. OpenMPS allows us to represent state vectors compactly, with matrix product states [55]. This Schmidt truncation enables us to test the quantum entangled breather's robustness [Fig. 4(d)].

Throughout this work, fits are made via standard chi-squared minimization routines. Such fits appear in the Brody-parameter estimation of Fig. 4(a), the Page-curve ansatz of Fig. 4(c), and the entangled-breather lifetimes of Fig. 4(d). The standard error in the fit parameters is defined as the square-root of the diagonal entries of the fit-parameter covariance matrices. This prescription was used to calculated error bars for the Brody parameter and the entangled-breather lifetime. In the Page-curve fits, we illustrated with shaded bands the temporal fluctuations of data used to calculate the long-time averages. The fluctuations are defined as the standard deviations in the data used to calculate the averages. The shaded bands in Fig. 3(d)-(e) show the standard deviations in the network-measure data used to calculate the long-time averages shown with data points. Often, the standard deviations are smaller than the data points.

The bond-entropy fluctuations in Fig. 4(b) are smoothed with a moving average whose temporal window equals the system size, L. The data shown come from $L = 19$. Therefore, a 19-time-step window low-pass-filters the data. Numerical derivatives amplify high-frequency fluctuations. Hence filtering is important for observing lower-frequency trends. We visualize the smoothing effect with faint lines that show the raw data, sampled every L time steps.

VI. PHYSICAL IMPLEMENTATION OF QUANTUM CELLULAR AUTOMATA

We prescribe a scheme for implementing QCA physically, beginning with general results before narrowing to an example platform. First, we show that the longitudinal-transverse quantum Ising model can, in a specific parameter regime, reproduce QCA dynamics. Many experimental platforms can simulate this Ising model and so can, in principle, simulate QCA. Examples include superconducting qubits, trapped ions, and Rydberg atoms.

We focus on Rydberg atoms trapped in an optical-tweezer lattice. The atoms interact through a van der Waals coupling that induces a Rydberg blockade: Two close-together atoms cannot be excited simultaneously. We exploit this blockade to condition a site's evolution on the site's neighbors. Moreover, Rydberg atoms can be arranged in various geometries subject to short- and long-range interactions [56]. We exploit these freedoms to engineer nearest-neighbor rules, with a linear atom chain and next-nearest-neighbor rules with a ladder-like lattice [Fig. 9(h)].

Related work appeared in the literature recently: A Rydberg-chain realization of QCA was proposed in [57]. Wintermantel *et al.* focus on 3-site neighborhoods and a spin-flip activation. The spin-flip QCA is closely related to classical cellular automata: Initial states on the Bloch sphere's poles remain on the poles. However, [57] involves applications to engineering entangled states. We present a general framework for Rydberg-atom QCA: Our proposal encompasses 3-site and 5-site neighborhoods, as well as entanglement-generating activation unitaries.

The present paper presents results about analog three-site-neighborhood QCA in only two sections; this is one of the two. Usually, we feature digital three-site-neighborhood QCA (T_R rules) and analog totalistic five-site-neighborhood QCA (F_R rules). These choices narrow down the plethora of possibilities to illustrative examples, though we tested many more possibilities and found similar results. Here, we discuss the analog three-site-neighborhood QCA, Eq. (7), to demonstrate our physical implementation's generality.

A. From QCA to the Ising model

In analog QCA, the Hermitian activation operator $\hat{h}_j = \hat{\sigma}_j^x$. According to Eq. (2), $\hat{h}_j$ contributes to the Hamiltonian if the neighboring sites satisfy the conditions imposed by the projectors. Such a state change can be modeled with the Ising Hamiltonian.

Let h_x denote the transverse field h_x; and h_z, the longitudinal field. The Ising Hamiltonian has the form

$$\hat{H} = h_x \sum_j \hat{\sigma}_j^x + h_z \sum_j \hat{\sigma}_j^z + \frac{J}{2} \sum_j \sum_{k \in \Omega_j} \hat{\sigma}_j^z \hat{\sigma}_k^z. \quad (18)$$

The interaction strength J is uniform across the neighbors $k \in \Omega_j$ and vanishes outside. If $h_x \ll J \approx h_z$, spin j evolves as though the other spins belonged to a static, classical external magnetic field, rather than to an interacting global quantum system. h_x serves as the jth qubit's gap frequency. $h_z + Jm$ serves as the effective external field's frequency. The magnetization $m = \left\langle \sum_{k \in \Omega_j} \hat{\sigma}_k^z \right\rangle$ counts the $|0\rangle$'s in Ω_j and subtracts off the number of $|1\rangle$'s.

Under each of several T_R rules, the activation operates only if a certain number of neighbors occupy $|1\rangle$'s: m must have a particular value. (Under each of the other T_R rules, the activation operates if m has one of several activating values.) Examples include T_1, T_6, and T_8. The Ising model can implement these rules if the longitudinal field's to $h_z = -mJ$. The central spin's oscillations will be resonant with the effective external field at the desired m value. If m does not have the desired value, the central spin's oscillations are strongly off-resonant. This off-resonance effects the projectors in Eq. (2). The central spin's maximum probability, across a Rabi cycle, of flipping is $h_x / \sqrt{h_x^2 + (h_z + Jm)^2}$. Rules that activate at multiple m values would require additional fields and resonances [57]. Examples include rule T_{14}, which activates when $m = 0, 2$.

B. From the Ising Model to the Rydberg-atom quantum simulator

Each atom has a ground state $|g\rangle$ coupled to a highly excited Rydberg state $|r\rangle$ of principle quantum number $\gg 1$. Atoms j and $k \neq j$ experience the isotropic van der Waals interaction $V_{j,k} = C_6 / a_{j,k}^6$. C_6 denotes an experimental parameter; and $a_{j,k}$, the interatomic separation.

Rydberg atoms evolve under the effective Hamiltonian

$$\hat{H}_{\text{Ryd.}} = \frac{\Omega}{2} \sum_j \hat{\sigma}_j^x + \Delta \sum_j \hat{n}_j + \frac{1}{2} \sum_{j,k} V_{j,k} \hat{n}_j \hat{n}_k. \quad (19)$$

Ω denotes the Rabi frequency of the coupling between the ground and excited states. Δ denotes a detuning in the natural Hamiltonian that is transformed and approximated to yield Eq. (19). The detuning affects all atoms uniformly.

We map the Rydberg Hamiltonian onto the Ising Hamiltonian as follows. First, we set $\Omega = 2h_x$ and $\Delta = 2(h_z - 2rJ)$. $2r$ equals the number of neighbors $k \in \Omega_j$. Second, we set $V_{j,k} = 4J$ for the neighbors $k \in \Omega_j$ and $V_{j,k} = 0$ for all other k. The second condition is easily satisfied in a linear chain, if Ω_j consists of the nearest-neighbor sites. Next-nearest neighbors can be neglected due to the rapid decay, with separation, of the van der Waals interaction's strength. Modifying the lattice geometry, we show later, enables us to include next-nearest neighbors in Ω_j.

We numerically simulated an L=17-atom chain evolving under the Hamiltonian Eq. (19). The simulations show the equivalence of a Rydberg-atom simulator's dynamics and QCA. We focused on the analog versions of rules T_1, T_6, and F_4. The numerical parameters reflect the physics of ^{87}Rb atoms with the excited state $|r\rangle = |70S_{1/2}\rangle$, for which $C_6 = 863$ GHz μm^6. We fixed $\Omega = 2$ MHz and $V_{j,j+1} = 36$ MHz, which correspond to an interatomic distance of $a \simeq 5.4$ μm, such that $V_{j,j+1} \gg \Omega$.

We simulated interactions within each QCA neighborhood, as well as interactions with the closest neighbors outside the neighborhood. The latter, we checked, do not significantly alter the dynamics. The QCA, recall, has boundary sites set to $|0\rangle$'s. We implemented these boundary conditions by tailoring the external field Δ experienced by the boundary sites.

The numerical results are shown in the top row in Fig 9. The Rydberg-atom dynamics agree strongly with the QCA. Thus, Rydberg atoms offer promise for quantum simulation of QCA and for studying QCA's robustness with respect to physical-implementation details.

C. Analog T-type implementation

Here, we introduce implementations of several analog T_R rules: T_6, T_1 and T_8. Under these rules, a neighborhood's central spin is activated if $m = 2, 0, -2$, respectively. Consider a linear atom chain with interatomic distance $a_{j,j+1} = a \; \forall j$ in the Rydberg-blockade regime [Fig. 9(g)]. Appropriately setting the detuning Δ can enhance the oscillations undergone by a neighborhood's central spin, conditionally on the spin's neighbors.

Figure 9 shows the numerically computed evolution. The system was initialized with one $|1\rangle$ centered in $|0\rangle$'s. Rule-T_1 simulations are depicted in Figs. 9(a)-(b); and rule-T_6 simulations, in Figs. 9(c)-(d). The QCA simulations (depicted on the left-hand side of each figure pair) agree qualitatively with the Rydberg simulations (depicted on the right-hand side).

The analog version of rule T_1 evolves the system under the Hamiltonian

$$\hat{H} = \sum_j \hat{P}_{j-1}^{(0)} \hat{\sigma}_j^x \hat{P}_{j+1}^{(0)}. \quad (20)$$

The projectors' action is implemented with the Ising

Hamiltonian when the resonance condition is imposed between $|000\rangle_{\Omega_j}$ and $|010\rangle_{\Omega_j}$. In each of these states, two neighbors occupy $|0\rangle$; two neighbors point upward; the magnetization $m = 2$. Hence the resonance condition implies that $h_z = -2J$, or $\Delta = -2V_{j,j+1}$. Rule T_8 effects the Hamiltonian Eq. (20), except each $\hat{P}^{(0)}$ is replaced with a $\hat{P}^{(1)}$. Hence $m = -2$, and $h_z = 2J$, i.e., $\Delta = 0$.

The Goldilocks rule T_6 evolves the system under the Hamiltonian

$$\hat{H} = \sum_j \left(\hat{P}^{(0)}_{j-1} \hat{\sigma}^x_j \hat{P}^{(1)}_{j+1} + \hat{P}^{(1)}_{j-1} \hat{\sigma}^x_j \hat{P}^{(0)}_{j+1} \right) . \qquad (21)$$

The resonance must be enhanced when the neighboring sites satisfy $m = 0$. Hence we set $h_z = 0$ or, equivalently, $\Delta = -V_{j,j+1}$ in the Rydberg Hamiltonian.

D. F-type implementation

Simulating the F-rules with Rydberg atoms requires that excited next-nearest-neighbor atoms have the same interaction energy as nearest-neighbor atoms. One can meet this condition by forming a zigzag lattice, as shown in Fig. 9(h). The distance $a_{\rm nn}$ between next-nearest-neighbor atoms equals the distance between next-nearest-neighbor atoms. Hence the interaction energies are $V_{j,j+1} = V_{\rm nn} \equiv V$.

We discuss, as an example, the F_4 rule's implementation. A neighborhood's central spin must oscillate if two of its four neighbors are excited. As for T_6, $m = 0$, leading to the resonance condition $\Delta = -2V$. Figure 9(e)-(f) depict the numerical results, and Fig. 9(h) depicts the atomic arrangement. The plots confirm strong qualitative agreement between the QCA dynamics and the quantum-simulator dynamics.

VII. CONCLUSIONS

We have discovered a physically potent feature of entangled quantum cellular automata: the emergence of complexity under Goldilocks rules. Goldilocks rules balance activity and inactivity. This tradeoff produces new, highly entangled, yet highly structured, quantum states. These states are persistently dynamic and neither uniform nor random. The two Goldilocks rules focused on here—T_6 for the 3-site-neighborhood QCA and F_4 for the 5-site-neighborhood QCA—activate a neighborhood's center site when the neighbors are half in $|1\rangle$'s and half in $|0\rangle$'s. Complexity signatures of Goldilocks rules include complex-network structure, high clustering and high disparity fluctuations; persistent entropy fluctuations; and robust emergent features, such as quantum entangled breathers. Non-Goldilocks rules still display interesting dynamical features. Indeed, the PXP model, equivalent to rule T_1, has received much attention in the literature and serves as an edge case, showing
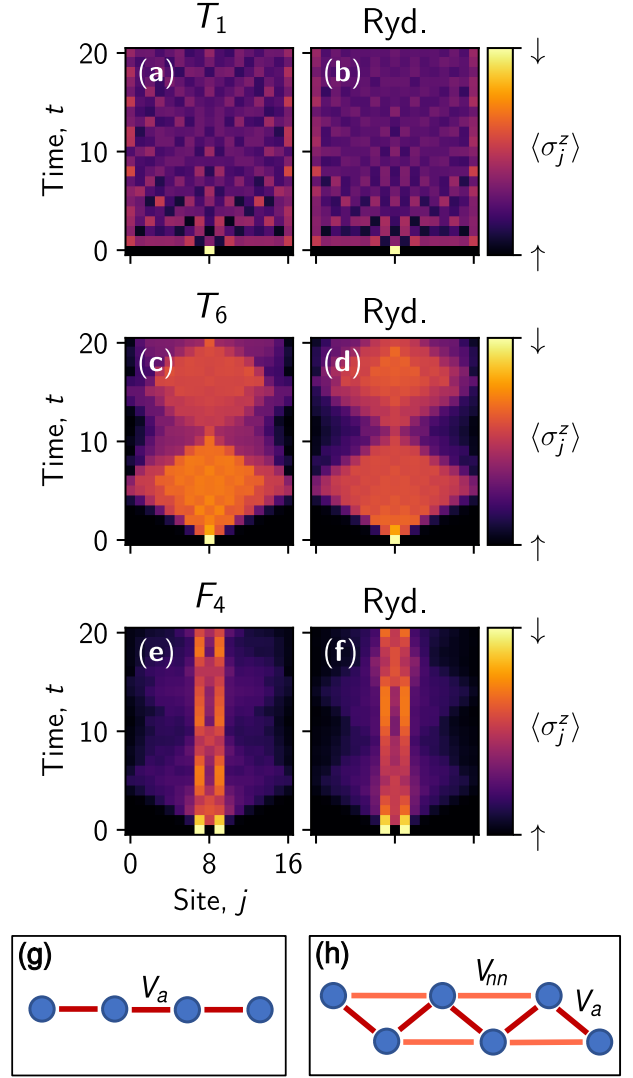

FIG. 9. Upper panel: Comparison of QCA evolution and Rydberg-atom-quantum-simulator dynamics. We study the rules T_1 (a)-(b) and T_6 (c)-(d), whose dynamics are generated for a linear atom chain (g) with an appropriate detuning. We study also rule F_4 (e)-(f), for which the lattice has the shape in (h): Two parallel chains of atoms, represented by circles, are trapped in a plane. The nearest-neighbor distance a (red lines) equals the next-nearest-neighbor distance nn (orange lines), so $V_a = V_{nn}$. A local detuning is applied at the boundaries to simulate the QCA boundary conditions. The higher-order effects of next-nearest-neighbor interactions (for rules T_1 and T_6) and next-next-nearest-neighbor interactions (for rule F_4) are simulated. Parameters: $L = 17$. In the Rydberg simulations, $\Omega = 2$ MHz, and $V_a = 36$ MHz. Time is expressed in units of 2π μs.

some persistent dynamical features. However, the confluence of several complexity signatures distinguishes the Goldilocks rules.

Moreover, we have demonstrated that our QCA time-evolution protocols are implementable in extant digital and analog quantum computers. In particular, we have

shown that Rydberg atom arrays can be arranged to engineer five-site QCA neighborhoods, large enough to support a robust quantum entangled breather. Digital quantum computers, programmed with discrete gate sequences, can also simulate QCA dynamics that support emergent complexity even with three-site neighborhoods. Our work uncovers a direction for quantum computation: to demonstrate that the rich features of biological and social complexity manifest in abiological quantum systems.

ACKNOWLEDGMENTS

Conceptualization (LDC); Data Curation (LEH, MTJ, DLV, PR); Formal Analysis (LEH, MTJ, DLV, PR, NYH, SN, SM, LDC); Funding Acquisition (SM, LDC); Investigation (all authors); Methodology (LEH, NYH, NB, SM, LDC); Project Administration (LDC); Resources (LDC); Software (LEH, MTJ, DLV, PR); Supervision (NYH, SM, NB, LDC); Validation (LEH, LDC); Writing - original draft (LEH, LDC); Writing - review & editing (LEH, MTJ, PR, NYH, NB, SN, SM, LDC).

Appendix: Cluster-state mutual information

A cluster state's mutual-information adjacency matrix forms a graph that can have more links than the original graph that defined the cluster state. For example, consider a three-qubit cluster state defined by a 3×1 grid (a 1D chain). The state vector is

$$
|\psi\rangle = \frac{1}{2^{3/2}} \begin{pmatrix} 1 \\ 1 \\ 1 \\ e^{iv} \\ 1 \\ 1 \\ e^{iv} \\ e^{2iv} \end{pmatrix}.
$$

The 1-site and 2-site reduced density matrices are

$$
\hat{\rho}_0 = \hat{\rho}_2 = \frac{1}{4} \begin{pmatrix} 2 & 1 + e^{-iv} \\ 1 + e^{iv} & 2 \end{pmatrix},
$$

$$
\hat{\rho}_1 = \frac{1}{8} \begin{pmatrix} 4 & (1 + e^{-iv})^2 \\ (1 + e^{iv})^2 & 4 \end{pmatrix},
$$

$$
\hat{\rho}_{0,1} = \frac{1}{8} \begin{pmatrix} 2 & 1 + e^{-iv} & 2 & e^{-iv} + e^{-2iv} \\ 1 + e^{iv} & 2 & 1 + e^{iv} & 2e^{-iv} \\ 2 & 1 + e^{-iv} & 2 & e^{-iv} + e^{-2iv} \\ e^{iv} + e^{2iv} & 2e^{iv} & e^{iv} + e^{2iv} & 2 \end{pmatrix},
$$

and,

$$
\hat{\rho}_{0,2} = \frac{1}{8} \begin{pmatrix} 2 & 1 + e^{-iv} & 1 + e^{-iv} & 1 + e^{-2iv} \\ 1 + e^{iv} & 2 & 2 & 1 + e^{-iv} \\ 1 + e^{iv} & 2 & 2 & 1 + e^{-iv} \\ 1 + e^{2iv} & 1 + e^{iv} & 1 + e^{iv} & 2 . \end{pmatrix}.
$$

$$\tag{A.1}$$

We index rows and columns such that $(0,0)$ appears in the upper left-hand corner. The reduced density matrix $\hat{\rho}_{1,2}$ equals the result of taking $\hat{\rho}_{0,1}$, swapping row 1 with row 2, and swapping column 1 with column 2. Diagonalizing these density matrices yields the entanglement spectra $\{\lambda_\pm\}$ for $\hat{\rho}_0$ and $\hat{\rho}_2$, as well as $\{\lambda_\pm, 0, 0\}$ for $\hat{\rho}_{0,1}$ and $\hat{\rho}_{1,2}$. The $\lambda_\pm = [1 \pm |\cos(v/2)|]/2$. Zero-valued eigenvalues do not contribute to the entropy, so

$$
s_0^{(2)} = s_2^{(2)} = s_{0,1}^{(2)} = s_{1,2}^{(2)} = 2 - \log_2 (3 + \cos v), \quad \text{(A.2)}
$$

wherein $v \in [0, 2\pi)$. The entanglement spectrum of $\hat{\rho}_1$ is $\{\lambda_1, \lambda_2\} = \{(1 - \cos v)/4, \ (3 + \cos v)/4\}$, and the entanglement spectrum of $\hat{\rho}_{0,2}$ is $\{\lambda_1, \ \lambda_2 \ 0, \ 0\}$. Hence the remaining entropies are

$$
s_1^{(2)} = s_{0,2}^{(2)} = 3 - \log_2 \left(5 + 2 \cos v + \cos^2 v \right). \quad \text{(A.3)}
$$

The mutual-information adjacency matrices' nonzero entropies can be expressed as $M_{0,1}^{(2)} = M_{1,0}^{(2)} = M_{1,2}^{(2)} = M_{2,1}^{(2)} = s_1^{(2)}/2$ and $M_{0,2}^{(2)} = M_{2,0}^{(2)} = s_0^{(2)} - s_1^{(2)}/2$.

The graph that defines the cluster state lacked a link between nodes 0 and 2. The nodes share mutual information, however: $M_{0,2} \neq 0$. For the same reason, the 1×19 cluster state of Fig. 3 has a large clustering and an intuitively large disparity.

[1] P. Arrighi, An overview of quantum cellular automata, Natural Computing **18**, 885 (2019).

[2] P. W. Anderson, *Basic Notions of Condensed Matter Physics* (Addison-Wesley, New York, 1984).

[3] M. E. J. Newman, The Structure and Function of Complex Networks, SIAM Review **45**, 167 (2003).

[4] M. E. Csete and J. C. Doyle, Reverse engineering of biological complexity, Science **5560**, 1664 (2002).

[5] S. Wolfram, Statistical mechanics of cellular automata, Rev. Mod. Phys. **55**, 601 (1983).

[6] E. Altman, K. R. Brown, G. Carleo, L. D. Carr, E. Demler, C. Chin, B. DeMarco, S. E. Economou, M. A. Eriksson, K.-M. C. Fu, M. Greiner, K. R. A. Hazzard, R. G. Hulet, A. J. Kollar, B. L. Lev, M. D. Lukin, R. Ma, X. Mi, S. Misra, C. Monroe, K. Murch, Z. Nazario, K.-K. Ni, A. C. Potter, P. Roushan, M. Saffman, M. Schleier-Smith, I. Siddiqi, R. Simmonds, M. Singh, I. B. Spielman, K. Temme, D. S. Weiss, J. Vuckovic, V. Vuletic, J. Ye, and M. Zwierlein, Quantum simulators: Architectures and opportunities (2019), arXiv:1912.06938 [quant-ph].

[7] H. Bernien, S. Schwartz, A. Keesling, H. Levine, A. Omran, H. Pichler, S. Choi, A. S. Zibrov, M. Endres, M. Greiner, *et al.*, Probing many-body dynamics on a 51-atom quantum simulator, Nature **551**, 579 (2017).

[8] Materials and methods are available as supplementary materials at the Science website.

[9] D. Bleh, T. Calarco, and M. S, Quantum game of life, Europhysics Letters **97**, 20012 (2012).

[10] L. E. Hillberry, *Entanglement and complexity in quantum elementary cellular automata*, Master's thesis, Colorado School of Mines. Arthur Lakes Library (2016).

[11] D. L. Vargas, *Quantum complexity: Quantum mutual information, complex networks, and emergent phenomena in quantum cellular automata*, Master's thesis, Colorado School of Mines. Arthur Lakes Library (2016).

[12] E. Bullmore and O. Sporns, Complex brain networks: graph theoretical analysis of structural and functional systems, Neuroscience **10**, 186 (2009).

[13] H. Weimer, M. Müller, I. Lesanovsky, P. Zoller, and H. P. Büchler, A Rydberg quantum simulator, Nature Physics **6**, 382 (2010).

[14] R. Blatt and C. F. Roos, Quantum simulations with trapped ions, Nature Physics **8**, 277 (2012).

[15] J. Zhang, G. Pagano, P. W. Hess, A. Kyprianidis, P. Becker, H. Kaplan, A. V. Gorshkov, Z. X. Gong, and C. Monroe, Observation of a many-body dynamical phase transition with a 53-qubit quantum simulator, Nature **551**, 601 (2017).

[16] F. Arute, K. Arya, R. Babbush, D. Bacon, J. C. Bardin, R. Barends, R. Biswas, S. Boixo, F. G. Brandao, D. A. Buell, *et al.*, Quantum supremacy using a programmable superconducting processor, Nature **574**, 505 (2019).

[17] I. Buluta and F. Nori, Quantum Simulators, Science **326**, 108 (2009).

[18] P. Hauke, F. M. Cucchietti, L. Tagliacozzo, I. Deutsch, and M. Lewenstein, Can one trust quantum simulators?, Reports on Progress in Physics **75**, 082401 (2012).

[19] A. Polkovnikov, K. Sengupta, A. Silva, and M. Vengalattore, Colloquium: Nonequilibrium dynamics of closed interacting quantum systems, Rev. Mod. Phys. **83**, 863 (2011).

[20] G. Grössing and A. Zeilinger, Quantum cellular automata, Complex systems **2**, 197 (1988).

[21] C. S. Lent, P. D. Tougaw, W. Porod, and G. H. Bernstein, Quantum cellular automata, Nanotechnology **4**, 49 (1993).

[22] D. A. Meyer, From quantum cellular automata to quantum lattice gases, Journal of Statistical Physics **85**, 551 (1996).

[23] P. D. Tougaw and C. S. Lent, Dynamic behavior of quantum cellular automata, Journal of Applied Physics **80**, 4722 (1996).

[24] T. Farrelly, A review of quantum cellular automata (2019), arXiv:1904.13318 [quant-ph].

[25] J. Haah, L. Fidkowski, and M. B. Hastings, Nontrivial quantum cellular automata in higher dimensions (2018), arXiv:1812.01625 [quant-ph].

[26] M. Freedman and M. B. Hastings, Classification of quantum cellular automata (2019), arXiv:1902.10285 [quant-ph].

[27] M. Freedman, J. Haah, and M. B. Hastings, The group structure of quantum cellular automata (2019), arXiv:1910.07998 [quant-ph].

[28] J. Haah, Clifford quantum cellular automata: Trivial group in 2d and witt group in 3d (2019), arXiv:1907.02075 [quant-ph].

[29] D. Gottesman, The heisenberg representation of quantum computers (1998), arXiv:quant-ph/9807006 [quant-ph].

[30] G. Brennen and J. Williams, Entanglement dynamics in one-dimensional quantum cellular automata, Phys. Rev. A **68**, 042311 (2003).

[31] J. Gütschow, S. Uphoff, R. F. Werner, and Z. Zimborás, Time asymptotics and entanglement generation of clifford quantum cellular automata, Journal of Mathematical Physics **51**, 015203 (2010).

[32] S. Gopalakrishnan and B. Zakirov, Facilitated quantum cellular automata as simple models with non-thermal eigenstates and dynamics, Quantum Science and Technology **3**, 044004 (2018).

[33] S. Gopalakrishnan, Operator growth and eigenstate entanglement in an interacting integrable floquet system, Phys. Rev. B **98**, 060302 (2018).

[34] C. W. von Keyserlingk, T. Rakovszky, F. Pollmann, and S. L. Sondhi, Operator hydrodynamics, otocs, and entanglement growth in systems without conservation laws, Phys. Rev. X **8**, 021013 (2018).

[35] J. Fitzsimons, L. Xiao, S. C. Benjamin, and J. A. Jones, Quantum information processing with delocalized qubits under global control, Phys. Rev. Lett. **99**, 030501 (2007).

[36] J. M. Carlson and J. Doyle, Complexity and robustness, Proceedings of the national academy of sciences **99**, 2538

(2002).

[37] C. Turner, A. Michailidis, D. Abanin, M. Serbyn, and Z. Papić, Quantum scarred eigenstates in a rydberg atom chain: Entanglement, breakdown of thermalization, and stability to perturbations, Physical Review B **98**, 155134 (2018).

[38] I. Lesanovsky, K. Macieszczak, and J. P. Garrahan, Non-equilibrium absorbing state phase transitions in discrete-time quantum cellular automaton dynamics on spin lattices, Quantum Science and Technology **4**, 02LT02 (2019).

[39] F. Lederer, G. I. Stegeman, D. N. Christodoulides, G. Assanto, M. Segev, and Y. Silberberg, Discrete solitons in optics, Physics Reports **463**, 1 (2008).

[40] D. Awschalom, K. K. Berggren, H. Bernien, S. Bhave, L. D. Carr, P. Davids, S. E. Economou, D. Englund, A. Faraon, M. Fejer, S. Guha, M. V. Gustafsson, E. Hu, L. Jiang, J. Kim, B. Korzh, P. Kumar, P. G. Kwiat, M. Lonar, M. D. Lukin, D. A. B. Miller, C. Monroe, S. W. Nam, P. Narang, J. S. Orcutt, M. G. Raymer, A. H. Safavi-Naeini, M. Spiropulu, K. Srinivasan, S. Sun, J. Vukovi, E. Waks, R. Walsworth, A. M. Weiner, and Z. Zhang, Development of quantum interconnects for next-generation information technologies (2019), arXiv:1912.06642 [quant-ph].

[41] M. A. Valdez, D. Jaschke, D. L. Vargas, and L. D. Carr, Quantifying complexity in quantum phase transitions via mutual information complex networks, Physical Review Letters **119** (2017).

[42] B. Sundar, M. A. Valdez, L. D. Carr, and K. R. A. Hazzard, Complex-network description of thermal quantum states in the ising spin chain, Phys. Rev. A **97**, 052320 (2018).

[43] Z.-C. Yang, A. Hamma, S. M. Giampaolo, E. R. Mucciolo, and C. Chamon, Entanglement complexity in quantum many-body dynamics, thermalization, and localization, Phys. Rev. B **96**, 020408 (2017).

[44] M. A. Valdez, G. Shchedrin, M. Heimsoth, C. E. Creffield, F. Sols, and L. D. Carr, Many-body quantum chaos and entanglement in a quantum ratchet, Phys. Rev. Lett. **120**, 234101 (2018).

[45] M. Costa, A. L. Goldberger, and C.-K. Peng, Multiscale entropy analysis of biological signals, Physical review E **71**, 021906 (2005).

[46] J. Eisert, M. Cramer, and M. B. Plenio, Colloquium: Area laws for the entanglement entropy, Reviews of Modern Physics **82**, 277 (2010).

[47] Y. O. Nakagawa, M. Watanabe, H. Fujita, and S. Sugiura, Universality in volume-law entanglement of scrambled pure quantum states, Nature communications **9**, 1 (2018).

[48] This is one of the two paper sections that reports on analog three-site QCA. Most of the paper illustrates with digital three-site QCA and analog five-site QCA. We focus on these two examples to whittle down the cornucopia of possibilities: Many combinations of neighborhood sizes, time-evolution schemes, etc. are possible; one paper can not report on all the combinations. We studied diverse combinations and found results consistent with the two illustrations in this paper. We discuss analog three-site QCA here because they are the analog QCA equivalent to three-site digital QCA.

[49] T. Brydges, A. Elben, P. Jurcevic, B. Vermersch, C. Maier, B. P. Lanyon, P. Zoller, R. Blatt, and C. F. Roos, Probing rényi entanglement entropy via randomized measurements, Science **364**, 260 (2019).

[50] This difference approximates a time derivative. "Central" refers to the centeredness, about t_i, of the times t_{i+1} and t_{i-1} in Eq. (11). The derivative approximated is a first derivative. $\Delta s_A^{(\alpha)}(t_i)$ is called "second-order" because the approximation is correct to second order in the time step.

[51] C. Chamon, A. Hamma, and E. R. Mucciolo, Emergent irreversibility and entanglement spectrum statistics, Physical review letters **112**, 240501 (2014).

[52] T. A. Brody, J. Flores, J. B. French, P. Mello, A. Pandey, and S. S. Wong, Random-matrix physics: spectrum and strength fluctuations, Reviews of Modern Physics **53**, 385 (1981).

[53] L. Reichl, *The transition to chaos: conservative classical systems and quantum manifestations* (Springer Science & Business Media, 2013).

[54] M. M. Wolf, F. Verstraete, M. B. Hastings, and J. I. Cirac, Area laws in quantum systems: mutual information and correlations, Physical Review Letters **100**, 070502 (2008).

[55] D. Jaschke, M. L. Wall, and L. D. Carr, Open source matrix product states: Opening ways to simulate entangled many-body quantum systems in one dimension, Computer Physics Communications **225**, 59 (2018).

[56] C. Adams, J. Pritchard, and J. Shaffer, Rydberg atom quantum technologies, Journal of Physics B: Atomic, Molecular and Optical Physics **53**, 012002 (2019).

[57] T. Wintermantel, Y. Wang, G. Lochead, S. Shevate, G. Brennen, and S. Whitlock, Unitary and nonunitary quantum cellular automata with rydberg arrays, Physical Review Letters **124**, 070503 (2020).